BNL-222762-2022-JAAM

Magnetic freeze-out and anomalous Hall effect in ZrTe5

A. Gourgout, C. C. Homes

To be published in "npj Quantum Materials"

February 2022

Condensed Matter Physics and Materials Science Department

Brookhaven National Laboratory

U.S. Department of Energy

USDOE Office of Science (SC), Basic Energy Sciences (BES) (SC-22)

DISCLAIMER

Magnetic freeze-out and anomalous Hall effect in $ZrTe_5$

Adrien Gourgout,[1] Maxime Leroux,[2] Jean-Loup Smirr,[3] Maxime Massoudzadegan,[2] Ricardo P. S. M. Lobo,[1] David Vignolles,[2] Cyril Proust,[2] Helmuth Berger,[4] Qiang Li,[5] Genda Gu,[5] Christopher C. Homes,[5] Ana Akrap,[6] and Benoît Fauqué[3,*]

[1] *Laboratoire de Physique et d'Étude des Matériaux (ESPCI Paris - CNRS - Sorbonne Université), PSL Research University, 75005 Paris, France*
[2] *Laboratoire National des Champs Magnétiques Intenses (LNCMI-EMFL), CNRS ,UGA, UPS, INSA, Grenoble/Toulouse, France*
[3] *JEIP, USR 3573 CNRS, Collège de France, PSL Research University, 11, place Marcelin Berthelot, 75231 Paris Cedex 05, France*
[4] *IPHYS, EPFL, CH-1015 Lausanne, Switzerland*
[5] *Condensed Matter Physics and Materials Science Department, Brookhaven National Laboratory, Upton, New York 11973, USA*
[6] *Department of Physics, University of Fribourg, 1700 Fribourg, Switzerland*

(Dated: January 21, 2022)

The ultra-quantum limit is achieved when a magnetic field confines an electron gas in its lowest spin-polarised Landau level. Here we show that in this limit, electron doped $ZrTe_5$ shows a metal-insulator transition followed by a sign change of the Hall and Seebeck effects at low temperature. We attribute this transition to a magnetic freeze-out of charge carriers on the ionised impurities. This reduction of the charge carrier density gives way to an anomalous Hall response of the spin-polarised electrons. This behaviour, at odds with the usual magnetic freeze-out scenario, occurs in this Dirac metal because of its tiny Fermi energy, extremely narrow band gap and a large g-factor. We argue that this anomalous Hall contribution could be either intrinsic or extrinsic.

Introduction

In the presence of a magnetic field, the electronic spectrum of a three-dimensional electron gas (3DEGs) is quantized into Landau levels. When all the charge carriers are confined in the lowest Landau level—the so-called *quantum limit*—the kinetic energy of electrons is quenched. This favors the emergence of electronic instabilities, either driven by the electron-electron or electron-impurity interactions [1–4]. So far, the behavior of 3DEGs beyond their quantum limit has been explored in a limited number of low carrier density systems. Yet, different instabilities have been detected, such as a thermodynamic phase transition in graphite [5–8], a valley depopulation phase in bismuth [9, 10], and a metal-insulator transition (MIT) in narrow-gap doped semiconductors InSb [11] and InAs [12, 13]. The latter occurs when charge carriers are confined in the lowest spin-polarised Landau level – the ultra-quantum limit. This transition is generally attributed to the magnetic freeze-out effect where electrons are frozen on ionized impurities [4, 14].

Lately, low-doped Dirac and Weyl materials with remarkable field-induced properties were discovered [15–19]. Of particular interest is the case of $ZrTe_5$. The entrance into its quantum limit regime is marked by quasi quantized Hall (ρ_{xy}) [18] and thermoelectrical Hall conductivity (α_{xy}) [20], followed by a higher magnetic field transition [18, 21]. This phase transition has initially been attributed to the formation of a charge density wave (CDW) [18, 21, 22]. Such interpretation has been questioned because there is no thermodynamic evidence [23, 24] as expected for a CDW transition. Furthermore, $ZrTe_5$ displays a large anomalous Hall effect (AHE), even though it is a non-magnetic material [25–28].

Here we report electrical, thermo-electrical and optical conductivity measurements over a large range of doping, magnetic field, and temperature in electron-doped $ZrTe_5$. For the first time, we probe this system down to sub-Kelvin temperatures. This allows us to track the Fermi surface evolution of $ZrTe_5$ and explain the nature of this phase transition, as well as its links with the observed AHE. We show that the onset of the field-induced transition can be ascribed to the magnetic freeze-out effect. In contrast with usually reported results, we show that the freeze-out regime of $ZrTe_5$ is characterised by a sign change of the Hall and thermoelectric effects, followed by a saturating Hall conductivity. Our results show that the magnetic freeze-out effect differs in this Dirac material as a consequence of the tiny band gap and large g-factor of $ZrTe_5$, that favor both an extrinsic and an intrinsic AHE of the spin-polarised charge carriers.

Field induced transition in the ultra-quantum limit of $ZrTe_5$

Fig. 1a) shows the temperature dependence of the resistivity (ρ_{xx}) for four batches, labelled S_{1-4} respectively. At room temperature, $\rho_{xx} \approx 0.7$ mΩ.cm. With decreasing temperature, ρ_{xx} peaks at a temperature around which the Hall effect (ρ_{xy}) changes its sign, which is around 150 K for S_{3b} sample (see Fig. 1b)). Both shift to

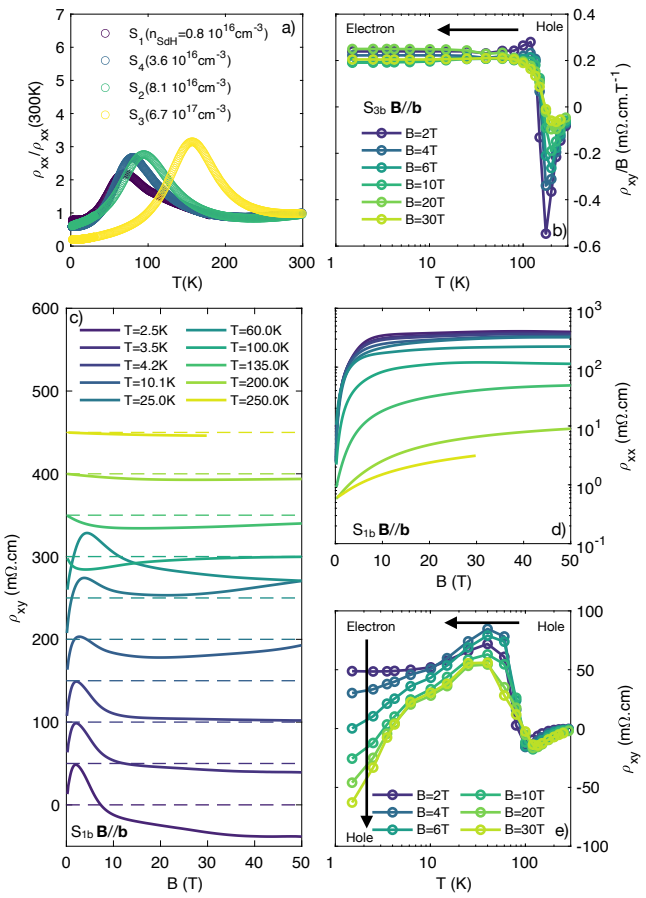

FIG. 1. **Resistivity (ρ_{xx}) and Hall effect (ρ_{xy}) of $ZrTe_5$: a) Temperature dependence of ρ_{xx} for the four different batches studied, labelled respectively $S_{1,2,3,4}$. n_{SdH} is the carrier density deduced from quantum oscillations (see [29]). b) $\frac{\rho_{xy}}{B}$ vs B for S_{3b} ($n_{S_3} = 6.7 \times 10^{17}cm^{-3}$). In all the field sweeps the magnetic field is parallel to the b-axis of the orthorhombic unit cell. c) ρ_{xy} vs B for sample S_{1b} for $T = 2.5$ K to 250 K. Curves are shifted for clarity. d) ρ_{xx} vs B for S_{1b} ($n_{S_1} = 0.8 \times 10^{16}cm^{-3}$). ρ_{xy} vs T for $B = 2$ T up to 30 T.**

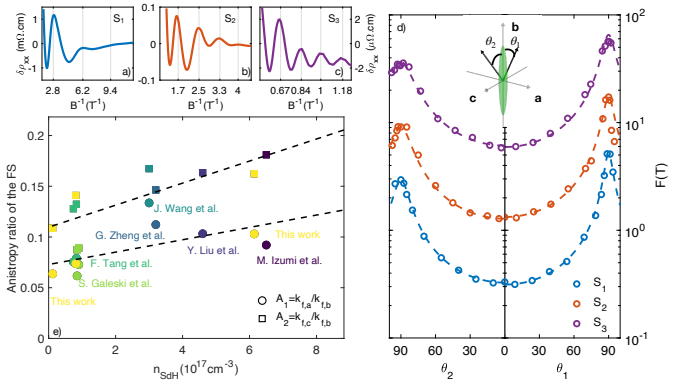

FIG. 2. **Doping evolution of the Fermi surface of $ZrTe_5$: a)-c) Trace of the Shubnikov-de Haas quantum oscillations measured in the three samples S_{1a}, S_{2a} and S_{3b} at $T = 2$ K for B ∥ b. d) Angular dependence of the frequency of quantum oscillations (F) in open circles as function of $\theta_{1,2}$, the angles between the b-axis and the magnetic field rotating in the (b,a) and (b,c) planes, respectively. The dotted lines are the frequency, F, for an ellipsoid Fermi surface of anisotropy A_i ($F = F_0(1+(1/A_i^2-1)cos^2(\theta))^{\frac{-1}{2}}$). For the two planes of rotations, A_i is given by $\frac{k_{f,a}}{k_{f,b}}$ and $\frac{k_{f,a}}{k_{f,c}}$, labelled A_1 and A_2 respectively. Their doping evolution is shown in e) and agrees well with the literature [18, 21, 23, 30–32].**

lower temperature as the carrier density decreases. These effects have been tracked by laser angle-resolved photoemission spectroscopy and attributed to a temperature-induced phase transition where the Fermi energy shifts from the top of the valence band to the bottom of the conduction band as the temperature decreases [33].

Fig. 1c) and d) show the field dependence of ρ_{xy} and ρ_{xx} up to 50 T for a magnetic field parallel to the b-axis of the orthorhombic unit cell. The data is shown for S_{1b} whose Hall carrier density is $n_H = 9 \times 10^{15}$ cm^{-3}, and Hall mobility, μ_H, is as large as 9.7×10^5 $V.cm^{-2}.s^{-1}$. At low temperatures ρ_{xx} increases by more than two orders of magnitude and saturates above ≈ 7 T. This large magnetoresistance vanishes as the temperature increases. Meanwhile, ρ_{xy} deviates from linearity above a few Tesla and changes sign around 7 T at low temperatures reminiscent of the sign change observed in temperature, see Fig. 1e). This field induced sign change of the Hall effect will be discussed in further details in the last section.

On top of this monotonic magnetoresistance, quantum oscillations are detected. Figs. 2a)-c) show the trace of these oscillations for samples from batches S_1, S_2 and S_3. In good agreement with previous measurements [30, 34] the Fermi surface of $ZrTe_5$ can be described as an anisotropic ellipsoid elongated along the b-axis, see Fig. 2d) and e). Our doping study reveals that the mass anisotropy ratio increases as the system is less doped and reach $\frac{m_b^*}{m_a^*} \simeq 250$ in our lowest doped samples, where $m^*_{a,b}$ are the band mass along the a and b axis. This large mass anisotropy ratio is comparable to the one of Dirac electrons of bismuth [35]. The Fermi surface mapping allows us to accurately determine the Fermi sea carrier densities, n_{SdH}, which agree well with n_H [29]. Remarkably, the last quantum oscillation occurs in S_1 samples at a small field of $B_{QL}(S_1) = 0.3$ T. Above this field, for $B > B_{QL}$, all the carriers are in the lowest spin-polarised $(0, -)$ Landau level. The insulating behavior of ρ_{xx} and the sign change of ρ_{xy} detected in Fig. 1d) and e), at low temperature, are thus properties which occur deep in the ultra-quantum regime.

Fig. 3 shows the doping evolution of ρ_{xx} and the subsequent field scale identified. A close inspection of the

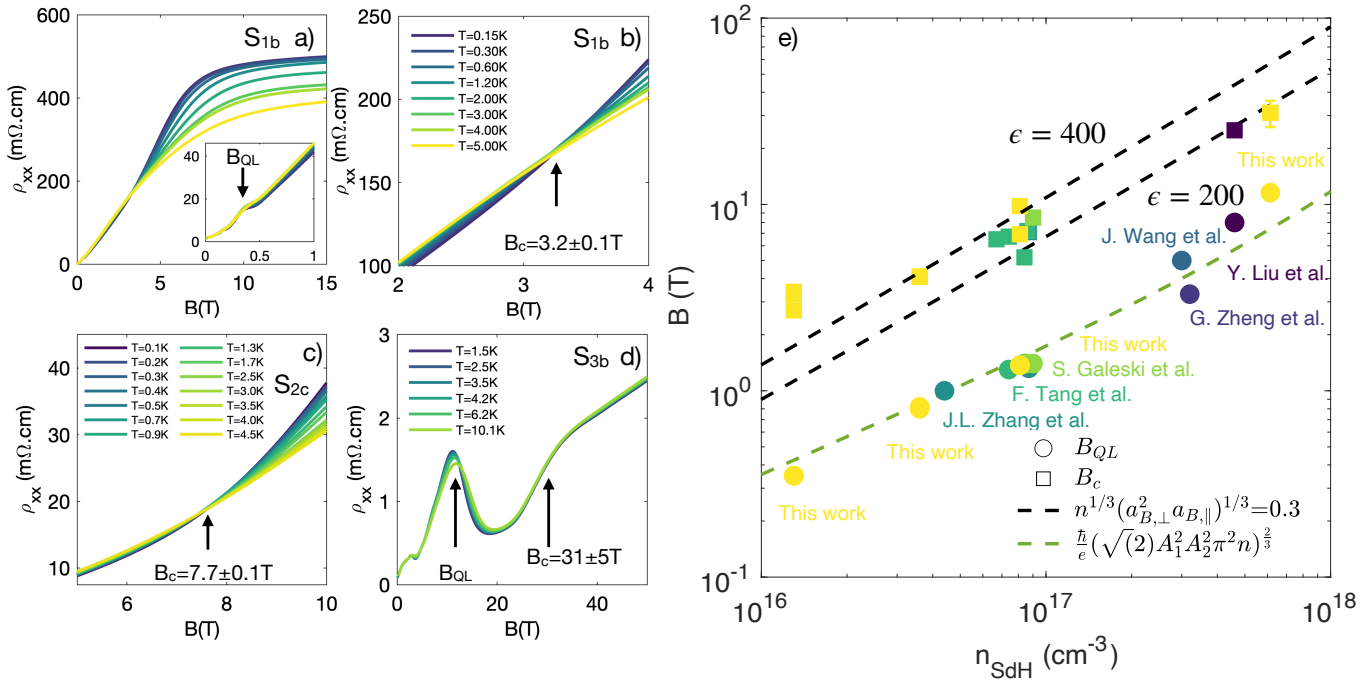

FIG. 3. **Doping evolution of the transition detected in the ultra-quantum regime of $ZrTe_5$. a) ρ_{xx} vs magnetic field for samples S_{1b}. Inset: same as a) up to 1 T. b) Same as a) with a zoom on the crossing point in ρ_{xx}. c), d) Same as a) for samples S_{2b} ad S_{3b}. At low doping the onset of the transition is marked by a crossing point. At the highest doping it evolves into a step in ρ_{xx}. e) Doping evolution of the position of the last quantum oscillation, B_{QL} (yellow closed circles) and the onset of the transition, B_c (yellow closed square) as determined in ρ_{xx} which agrre well with the result from the literature [18, 21, 23, 31, 32, 36]. The dashed green line in Fig. 3e) is the value of B_{QL} for an anisotropic ellipsoid (see the text). The dashed black lines are the onset of the magnetic freeze-out transition according to Eq. 1 with ϵ = 200 and 400.**

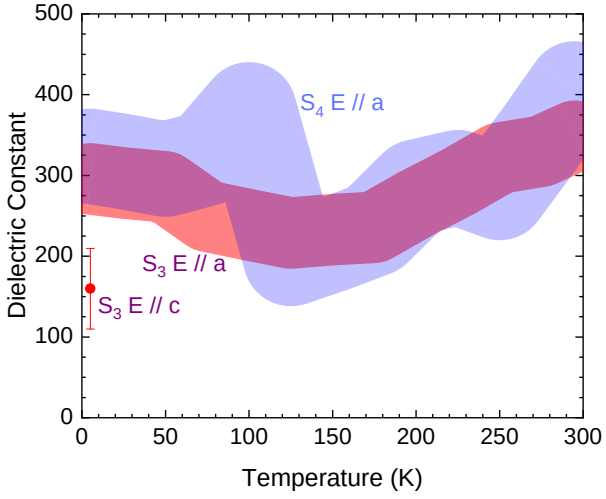

FIG. 4. **Temperature dependence of the dielectric constant ϵ for two samples from batch S_4 (n_{SdH}=3.6 $\times$ 10^{16}cm^{-3}) and S_3 (n_{SdH}=6.7 $\times$ 10^{17}cm^{-3}) for E $\parallel$ a and E $\parallel$ c (red point) of $ZrTe_5$.**

low temperature behavior of ρ_{xx} reveals a light metallic phase above B_{QL} (see Fig.3a) and b)) which ends at a crossing point at B_c = 3.2 T above which an insulating state is observed up to 50 T. Following [18] we take this crossing point as the onset of the metal-insulator transition. As the carrier density increases, both the position of B_{QL} and B_c increase (see Fig. 3b) and c)). At the highest doping (samples S_3) the amplitude of the magnetoresistance has decreased and the transition is only marked by a modest increase by a factor of two of ρ_{xx} at $\simeq$ 30 T, indicating that the transition smears with the doping increase (see Fig. 3d)). Fig. 3e) shows the doping evolution of B_{QL} and B_c which are in good agreement with previous works [18, 21, 23]. The dashed green line in Fig. 3e) is the carrier density dependence of B_{QL} for a 3D anisotropic Fermi surface with a Zeeman energy equal to the cyclotron energy. It is given by $B_{QL} = \frac{\hbar}{e}(\sqrt{(2)}\pi^2A_1^2A_2^2n)^{\frac{2}{3}}$, where A_1 and A_2 are the anisotropic Fermi momentum ratios between the a and b-axis, and between the c and b-axis. Plugging the doping evolution of $A_{1,2}$ shown in Fig 2e) provides an excellent agreement of the detected B_{QL}.

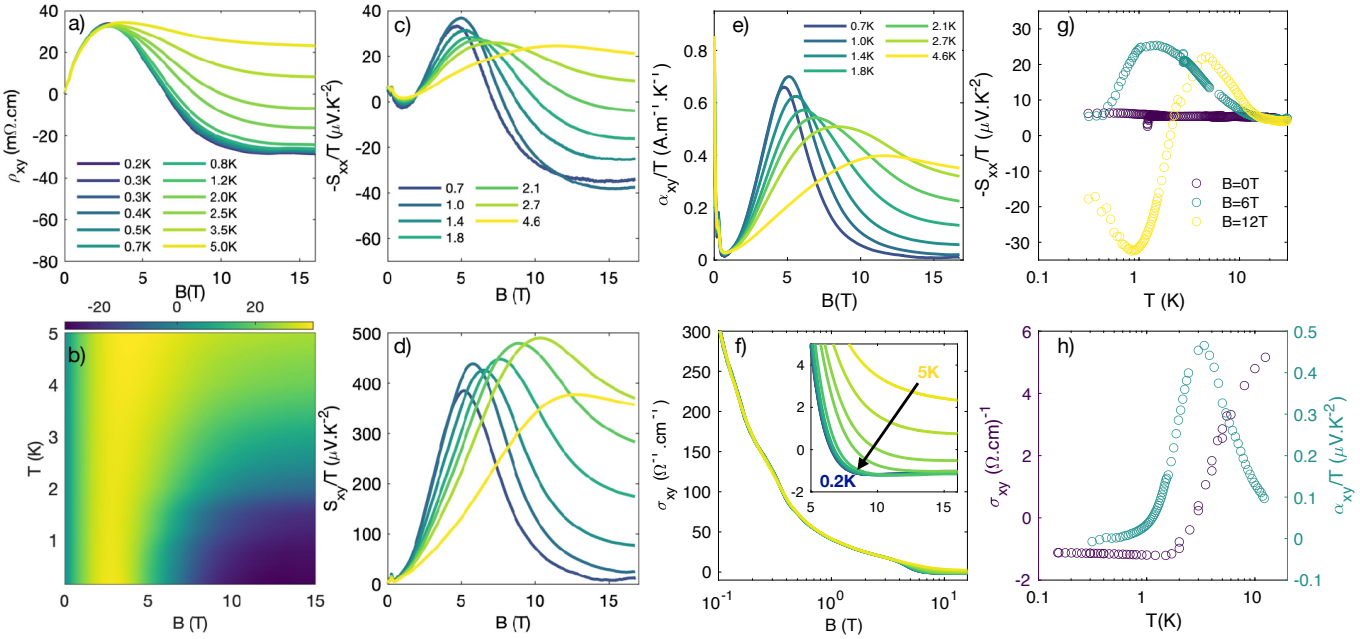

FIG. 5. **Electrical and thermoelectrical properties beyond B_c for S_{1c}: a) ρ_{xy} vs B. b) $T-B$ color map of ρ_{xy} deduced from a). c) and d) $-\frac{S_{xx}}{T}$ and $\frac{S_{xy}}{T}$ vs B from $T = 0.7$ K up to 4.8 K. e) and f) α_{xy}/T and Hall conductivity, σ_{xy}, vs B. Inset of f) : zoom of σ_{xy} from 5 to 16 T. g) Temperature dependence of $-\frac{S_{xx}}{T}$ at $B =$ 0, 6 and 12 T. h) Temperature dependence of σ_{xy} and $\frac{\alpha_{xy}}{T}$ at $B = 12$ T.**

Magnetic freeze-out in $ZrTe_5$

The doping evolution of B_c is a clue to the nature of this transition. So far it has been attributed to the formation of a charge density wave (CDW) along the magnetic field [18, 21, 22]. Such an instability is favored by the one-dimensional nature of the electronic spectrum along the magnetic field, which provides a suitable $(2k_F)$ nesting vector in the $(0,-)$ Landau level. In this picture, predicted long ago [37], the transition is of second order and is expected to vanish as the temperature increases. The absence of temperature dependence of B_c and the absence of thermodynamic signature [23, 24] invite us to consider another interpretation.

In the CDW picture, the instability is driven by the electron-electron [18, 21, 37] or electron-phonon interaction [22] and the interaction between electrons and the ionized impurities is neglected. However, in a doped semiconductor, the conduction band electrons are derived from uncompensated donors. Tellurium vacancies have been identified as the main source of impurities in $ZrTe_5$ flux samples [38, 39]. According to the Mott criterion [40, 41] a semiconductor becomes metallic when the density of its carriers, n, exceeds a threshold set by its effective Bohr radius, $a_B = 4\pi\varepsilon\hbar/m^*e^2$ (where m^* is the effective mass of the carrier, ε is the dielectric constant of the semiconductor): $n^{1/3}a_B \simeq 0.3$. In presence of a magnetic field the in-plane electronic wave extension shrinks with increasing magnetic field. When $B > B_{QL}$, the in-plane Bohr radius is equal to $a_{B,\perp} = 2\ell_B$ with $\ell_B = \sqrt{(\frac{\hbar}{eB})}$ [4, 42]. Along the magnetic field direction, the characteristic spatial extension is $a_{B,\parallel} = \frac{a_{B,z}}{\log(\gamma)}$, where $\gamma = (\frac{a_{B,c}}{l_B})^2$ and $a_{B,z,c}=\frac{\varepsilon}{m^*_{z,c}}a_{B,0}$ with $m^*_{z,c}$ is the mass along and perpendicular to the magnetic field, in units of m_0 and $a_{B,0}$ is the bare Bohr radius. A MIT transition is thus expected to occur when the overlap between the wave functions of electrons is sufficiently reduced [11, 14] i.e. when:

$$n^{1/3}(a^2_{B,\perp}a_{B,\parallel})^{\frac{1}{3}} \simeq 0.3 \qquad (1)$$

This MIT is thus a Mott transition assisted by the magnetic field where the metal is turned into an insulator due to the freezing of electrons on the ionized donors by the magnetic field, the so-called magnetic freeze-out effect. According to Eq. 1 $n \propto B_c/\log(B_c)$ and B_c is slightly sublinear in n and evolves almost parallel to B_{QL}. In order to test this scenario quantitatively, one has to determine the threshold of the transition from Eq. 1, which requires knowing ε and $m^*_{z,c}$. Temperature dependence of the quantum oscillations gives access to $m^*_z \approx 2m_0$ and $m^*_c \approx 0.02m_0$ for $\mathbf{B} \parallel \mathbf{b}$, while the optical reflectivity measurements give access to ε. Fig. 4 shows ε versus temperature for two samples of batches S_1 and S_3. ε is as large as 200-400ε_0 in $ZrTe_5$ (see [29] for further detail). The deduced onset from Eq. 1 is shown in dashed black lines in Fig. 3e) for $\varepsilon = 200$ and 400, capturing well the doping evolution of B_c. We thus attribute the transition

detected in the quantum limit of $ZrTe_5$ to the magnetic freeze-out effect.

It is worth noticing that a large contribution to ε comes from interband electronic transitions resulting in $\varepsilon_\infty > 100$, see [29]. This result also clarifies why one can detect highly mobile carriers even down to densities as low as 10^{13} cm^{-3} [28]. Due to its light in-plane carrier mass and large dielectric constant, one expects threshold of the MIT at zero magnetic field to be below $\approx 10^{12}$ cm^{-3}.

Anomalous Hall effect in $ZrTe_5$

The electronic properties above B_c contrast with the usual freeze-out scenario, such as observed in InSb (n_H= 2-5$\times 10^{15}$ cm^{-3}) [11], where an activated insulating behavior accompanies the large drop in carrier density. In $ZrTe_5$ we found a saturating ρ_{xx} and, more surprisingly, a sign change of ρ_{xy}, see Fig. 5a) and b). Study of the Seebeck (S_{xx}=$\frac{E_x}{\Delta_x T}$) and Nernst effect (S_{xy}=-$\frac{E_y}{\Delta_x T}$), further confirm the emergence of a low temperature energy scale above B_c.

Fig. 5c), d) and e) show the field dependence of S_{xx}/T, S_{xy}/T, and α_{xy}/T the transverse component of the thermoelectric tensor of sample S_{1c} (see [29] for similar result on S_{1b} sample). They all peak slightly above B_c revealing a breakdown of the thermoelectric Hall plateau observed above 5 K [20]. Above 7 T S_{xx}/T changes of sign as ρ_{xy}. Temperature dependence of S_{xx}/T is shown on Fig. 5g) for $B = 0$, 6 and 12 T. At $B = 0$ T, $S_{xx}/T = -5.5$ μV.K^{-2} in quantitative agreement with the expected value for the diffusive response of a degenerate semiconductor, which predicts $S_{xx}/T = \frac{-\pi^2}{2}\frac{k_B}{eT_F} = -5$ μV.K^{-2} for $T_F \approx 80$ K deduced from quantum oscillation measurements. At B = 12 T, the sign change of the Hall conductivity, σ_{xy}, at 3 K is accompanied by a peak in α_{xy}/T (see Fig. 5h)) and a sign change in S_{xx}/T (see Fig. 5g)). At the lowest temperature S_{xx}/T saturates to $\simeq +20$ μV.K^{-2}, a value four times larger than in zero magnetic field, pointing to a reduction of the charge carrier density by a factor of eight which should lead to an enhancement of ρ_{xy}. In stead, deep in the the freeze-out regime ($B >> B_c$), ρ_{xy} as well as σ_{xy} saturates as shown in Fig. 5f) reminiscent of an AHE.

Indeed, several studies have reported an AHE in $ZrTe_5$ [25–28]. In this case, the Hall conductivity is the sum of two contributions: $\sigma_{xy} = -\frac{ne}{B} + \sigma^A_{xy}$ where the first and second terms are the orbital conductivity and the anomalous Hall conductivity, respectively. At high enough magnetic field, when n decreases through the freeze-out transition, σ^A_{xy} becomes dominant, setting the amplitude and the sign of ρ_{xy}. So far, σ^A_{xy} has been attributed to the presence of a non-zero Berry curvature—an intrinsic effect—either due to the Weyl nodes in the band structure [25], or to the spin-split massive Dirac bands with non zero Berry curvature [27, 28]. In the latter case, σ^A_{xy} scales with the carrier density, and its amplitude is expected to be $+1$ (Ω.cm)$^{-1}$ for n_H=2 $\times$ 10^{16} cm^{-3} [27], which is of the same order of magnitude as our results. Skew and side jump scattering are another source of AHE in non magnetic semiconductors such as InSb [43, 44]. Deep in the freeze-out regime of low doped InSb ($n_H \approx 10^{14}$ cm^{-3}), a sign change of the Hall effect has been observed and attributed to skew scattering [45]. In contrast with dilute ferromagnetic alloys, where the asymmetric electron scattering is due to the spin-orbit coupling at the impurity sites, here it caused by the spin-polarised itinerant electron scattering off of ionized impurities. Its amplitude is given by σ^S_{xy}=$N_S e\frac{g^*\mu_B}{E_1}$, where E_1=$\frac{\epsilon_G(\epsilon_G+\Delta)}{2\epsilon_G+\Delta}$ with ϵ_G the band gap and Δ the spin-orbit splitting of the valence band. N_S is the density of scattering centers [44, 45]. Note that it induces a sign change of the Hall conductivity and it is only set by intrinsic parameters to the exception of N_S. Assuming $N_S \approx n_H$ and taking $g^* \approx 20$ [21, 32] and E_1=$\frac{\epsilon_G}{2}$ = 5 meV [46] ($\epsilon_G << \Delta$), we find that $\sigma^S_{xy} \simeq +1(\Omega.cm)^{-1}$, which is similar to the intrinsic contribution. Remarkably, it is four orders of magnitude larger than what has been observed in low doped InSb [45], due to the tiny gap and a (relatively) larger carrier density in $ZrTe_5$.

In summary, we show that the doping evolution of the onset transition detected in the ultra-quantum limit of $ZrTe_5$ can be ascribed to the magnetic freeze-out where electrons become bounded to donors. This MIT transition is marked by a peak in S_{xx}/T, S_{xy}/T and thus in α_{xy}/T, demonstrating the collapse of the thermoelectric Hall plateau [20] at low temperature. Beyond this transition, the Hall conductivity changes its sign at low temperature and becomes anomalous with a relatively large amplitude for this low carrier density and non magnetic material. Distinguishing and tuning both contributions by doping, pressure or strain is an appealing perspective for future research. To date, the AHE of the spin-polarised electrons in the ultra-quantum limit has been detected in a limited number of cases. Many Dirac materials with small gaps and large g-factors remain to be studied, in particular at higher doping where the intrinsic and extrinsic AHE are both expected to be larger.

Data avaliability

All data supporting the findings of this study are available from the corresponding author B.F. upon request.

Acknowledgments

We thank K. Behnia, J-H Chu, A. Jaoui, B. Skinner and B. Yang for useful discussions. We acknowledge the

support of the LNCMI-CNRS, member of the European Magnetic Field Laboratory (EMFL). This work was supported by JEIP-Collège de France, by the Agence Nationale de la Recherche (ANR-18-CE92-0020-01; ANR-19-CE30-0014-04) and by a grant attributed by the Ile de France regional council.

* benoit.fauque@espci.fr

[1] V. Celli and N. D. Mermin, Phys. Rev. **140**, A839 (1965).
[2] B. I. Halperin, Japanese Journal of Applied Physics **26**, 1913 (1987).
[3] A. H. MacDonald and G. W. Bryant, Phys. Rev. Lett. **58**, 515 (1987).
[4] Y. Yafet, R. Keyes, and E. Adams, Journal of Physics and Chemistry of Solids **1**, 137 (1956).
[5] B. Fauqué, D. LeBoeuf, B. Vignolle, M. Nardone, C. Proust, and K. Behnia, Phys. Rev. Lett. **110**, 266601 (2013).
[6] D. LeBoeuf, C. W. Rischau, G. Seyfarth, R. Küchler, M. Berben, S. Wiedmann, W. Tabis, M. Frachet, K. Behnia, and B. Fauque, Nature communications **8**, 1337 (2017).
[7] Z. Zhu, P. Nie, B. Fauqué, B. Vignolle, C. Proust, R. D. McDonald, N. Harrison, and K. Behnia, Phys. Rev. X **9**, 011058 (2019).
[8] C. Marcenat, T. Klein, D. LeBoeuf, A. Jaoui, G. Seyfarth, J. Kačmarčík, Y. Kohama, H. Cercellier, H. Aubin, K. Behnia, and B. Fauqué, Phys. Rev. Lett. **126**, 106801 (2021).
[9] Z. Zhu, J. Wang, H. Zuo, B. Fauqué, R. D. McDonald, Y. Fuseya, and K. Behnia, Nature Communications **8**, 15297 (2017).
[10] A. Iwasa, A. Kondo, S. Kawachi, K. Akiba, Y. Nakanishi, M. Yoshizawa, M. Tokunaga, and K. Kindo, Scientific Reports **9**, 1672 (2019).
[11] M. Shayegan, V. J. Goldman, and H. D. Drew, Phys. Rev. B **38**, 5585 (1988).
[12] L. A. Kaufman and L. J. Neuringer, Phys. Rev. B **2**, 1840 (1970).
[13] A. Jaoui, G. Seyfarth, C. W. Rischau, S. Wiedmann, S. Benhabib, C. Proust, K. Behnia, and B. Fauqué, npj Quantum Materials **5**, 94 (2020).
[14] B. A. Aronzon and I. M. Tsidilkovskii, Physica Status Solidi (b) **157**, 17 (1990).
[15] P. J. W. Moll, A. C. Potter, N. L. Nair, B. J. Ramshaw, K. A. Modic, S. Riggs, B. Zeng, N. J. Ghimire, E. D. Bauer, R. Kealhofer, F. Ronning, and J. G. Analytis, Nature Communications **7**, 12492 (2016).
[16] B. Ramshaw, K. Modic, A. Shekhter, Y. Zhang, E.-A. Kim, P. J. Moll, M. D. Bachmann, M. Chan, J. Betts, F. Balakirev, *et al.*, Nature communications **9**, 2217 (2018).
[17] S. Liang, S. Kushwaha, T. Gao, M. Hirschberger, J. Li, Z. Wang, K. Stolze, B. Skinner, B. A. Bernevig, R. J. Cava, *et al.*, Nature materials **18**, 443 (2019).
[18] F. Tang, Y. Ren, P. Wang, R. Zhong, J. Schneeloch, S. A. Yang, K. Yang, P. A. Lee, G. Gu, Z. Qiao, and L. Zhang, Nature **569**, 537 (2019).
[19] J. Gooth, B. Bradlyn, S. Honnali, C. Schindler, N. Kumar, J. Noky, Y. Qi, C. Shekhar, Y. Sun, Z. Wang, B. A. Bernevig, and C. Felser, Nature **575**, 315 (2019).
[20] W. Zhang, P. Wang, B. Skinner, R. Bi, V. Kozii, C.-W. Cho, R. Zhong, J. Schneeloch, D. Yu, G. Gu, L. Fu, X. Wu, and L. Zhang, Nature Communications **11**, 1046 (2020).
[21] Y. Liu, X. Yuan, C. Zhang, Z. Jin, A. Narayan, C. Luo, Z. Chen, L. Yang, J. Zou, X. Wu, S. Sanvito, Z. Xia, L. Li, Z. Wang, and F. Xiu, Nature Communications **7**, 12516 (2016).
[22] F. Qin, S. Li, Z. Z. Du, C. M. Wang, W. Zhang, D. Yu, H.-Z. Lu, and X. C. Xie, Phys. Rev. Lett. **125**, 206601 (2020).
[23] S. Galeski, T. Ehmcke, R. Wawrzyńczak, P. M. Lozano, K. Cho, A. Sharma, S. Das, F. Küster, P. Sessi, M. Brando, R. Küchler, A. Markou, M. König, P. Swekis, C. Felser, Y. Sassa, Q. Li, G. Gu, M. V. Zimmermann, O. Ivashko, D. I. Gorbunov, S. Zherlitsyn, T. Förster, S. S. P. Parkin, J. Wosnitza, T. Meng, and J. Gooth, Nature Communications **12**, 3197 (2021).
[24] Y. Tian, N. Ghassemi, and J. H. Ross, Phys. Rev. Lett. **126**, 236401 (2021).
[25] T. Liang, Q. Gibson, J. Xiong, M. Hirschberger, S. P. Koduvayur, R. J. Cava, and N. P. Ong, Nature communications **4**, 2696 (2013).
[26] Z. Sun, Z. Cao, J. Cui, C. Zhu, D. Ma, H. Wang, W. Zhuo, Z. Cheng, Z. Wang, X. Wan, and X. Chen, npj Quantum Materials **5**, 36 (2020).
[27] Y. Liu, H. Wang, H. Fu, J. Ge, Y. Li, C. Xi, J. Zhang, J. Yan, D. Mandrus, B. Yan, and J. Wang, Phys. Rev. B **103**, L201110 (2021).
[28] J. Mutch, X. Ma, C. Wang, P. Malinowski, J. Ayres-Sims, Q. Jiang, Z. Liu, D. Xiao, M. Yankowitz, and J.-H. Chu, "Abrupt switching of the anomalous hall effect by field-rotation in nonmagnetic zrte5," (2021), arXiv:2101.02681 [cond-mat.mes-hall].
[29] See Supplemental Material for more details on the samples, the comparison of quantum oscillations results, the thermal conductivity measurement, additional electrical thermoelectrical data sets and the determination of the dielectric constant.
[30] M. Izumi, T. Nakayama, K. Uchinokura, S. Harada, R. Yoshizaki, and E. Matsuura, Journal of Physics C: Solid State Physics **20**, 3691 (1987).
[31] G. Zheng, J. Lu, X. Zhu, W. Ning, Y. Han, H. Zhang, J. Zhang, C. Xi, J. Yang, H. Du, K. Yang, Y. Zhang, and M. Tian, Phys. Rev. B **93**, 115414 (2016).
[32] J. Wang, J. Niu, B. Yan, X. Li, R. Bi, Y. Yao, D. Yu, and X. Wu, Proceedings of the National Academy of Sciences **115**, 9145 (2018), https://www.pnas.org/content/115/37/9145.full.pdf.
[33] Y. Zhang, C. Wang, L. Yu, G. Liu, A. Liang, J. Huang, S. Nie, X. Sun, Y. Zhang, B. Shen, J. Liu, H. Weng, L. Zhao, G. Chen, X. Jia, C. Hu, Y. Ding, W. Zhao, Q. Gao, C. Li, S. He, L. Zhao, F. Zhang, S. Zhang, F. Yang, Z. Wang, Q. Peng, X. Dai, Z. Fang, Z. Xu, C. Chen, and X. J. Zhou, Nature Communications **8**, 15512 (2017).
[34] G. N. Kamm, D. J. Gillespie, A. C. Ehrlich, T. J. Wieting, and F. Levy, Phys. Rev. B **31**, 7617 (1985).
[35] Z. Zhu, B. Fauqué, Y. Fuseya, and K. Behnia, Phys. Rev. B **84**, 115137 (2011).
[36] J. L. Zhang, C. M. Wang, C. Y. Guo, X. D. Zhu, Y. Zhang, J. Y. Yang, Y. Q. Wang, Z. Qu, L. Pi, H.-Z. Lu, and M. L. Tian, Phys. Rev. Lett. **123**, 196602

(2019).
[37] N. D. Mermin and H. Wagner, Phys. Rev. Lett. **17**, 1133 (1966).
[38] P. Shahi, D. J. Singh, J. P. Sun, L. X. Zhao, G. F. Chen, Y. Y. Lv, J. Li, J.-Q. Yan, D. G. Mandrus, and J.-G. Cheng, Phys. Rev. X **8**, 021055 (2018).
[39] B. Salzmann, A. Pulkkinen, B. Hildebrand, T. Jaouen, S. N. Zhang, E. Martino, Q. Li, G. Gu, H. Berger, O. V. Yazyev, A. Akrap, and C. Monney, Phys. Rev. Materials **4**, 114201 (2020).
[40] N. F. Mott and E. Davis, *Electronic Processes in Non-Crystalline Materials* ((Oxford: Clarendon Press, 1971).
[41] N. F. Mott, *Metal-insulator transitions*, 2nd ed. (Taylor & Francis, London, 1990).
[42] B. I. Shklovskii and A. L. Efros, *Electronic properties of doped semiconductors* (Springer-Verlag, New York, 1984).
[43] J. N. Chazalviel and I. Solomon, Phys. Rev. Lett. **29**, 1676 (1972).
[44] Nozières, P. and Lewiner, C., J. Phys. France **34**, 901 (1973).
[45] H. Biernat and M. Kriechbaum, physica status solidi (b) **78**, 653 (1976).
[46] E. Martino, I. Crassee, G. Eguchi, D. Santos-Cottin, R. D. Zhong, G. D. Gu, H. Berger, Z. Rukelj, M. Orlita, C. C. Homes, and A. Akrap, Phys. Rev. Lett. **122**, 217402 (2019).

Supplementary Material for : "Magnetic freeze-out and anomalous Hall effect in $ZrTe_5$"

(Dated: January 21, 2022)

SAMPLES STUDIED

Two sets of samples have been used in this study. The first ones, grown by flux method where iodine served as a transport agent for the constituents, have the lowest carrier density. The second ones, grown by Chemical Vapor Transport (CVT), have the highest density. A samples list with their characteristic is shown in Tab. I. Samples from batch S_1, S_2 and S_4 have been grown by the flux method while samples from batch S_3 have been grown by CVT method.

Electrical and Hall resisitivity measurements have been measured using four point contacts. High magnetic field measurement has been done at LNCMI-Toulouse. Contact resistance of a less 1 Ω has been achieved by an Argon etching, follow by the deposit of 10 nm Ti buffer layer and of 150 nm Pd layer. Thermo-electrical and thermal transport measurements has been done used a standard two-thermoemeters one-heater set up similar to one used in [1].

Samples Name (Batch)	Size ($w \times t/L$) (mm)	ρ(2K) (mΩ.cm)	n_H(B− >0) (cm^{-3})	n_{SdH} (cm^{-3})	μ_H (V.cm^{-2}.s^{-1})
S_{1a}	0.44*0.17*3.9	1.76	1.2e16	0.8e16	3e5
S_{1b}	0.4*0.15*3.2	0.8	0.9e16	0.8e16	7.8e5
S_{1c}	0.55*0.14*2.8	0.44	1.6e16	0.8e16	9.7e5
S_{4a}	0.04*0.16*0.92	0.4	2e16	3.6e16	4.3e5
S_{2b}	0.03*0.14*1.0	0.31	1.2e17	8.1e16	1.6e5
S_{2c}	0.4*0.17*3.9	0.22	8.0e16	8.1e16	3.5e5
S_{3a}	0.14*0.028/1.0	0.091	1.4e18	6.1e17	4.9e4
S_{3b}	0.015*0.111/0.479	0.056	1.2e18	6.4e17	9.3e4

TABLE I: Table of the $ZrTe_5$ samples measured in our transport study. Hall mobilities at 2 K have been estimated according to the Drude expression : $\mu_H = \frac{1}{en_H\rho}$ where n_H and ρ are the low temperature Hall carrier densities and resistivities. n_{SdH} is the carrier density deduced from the quantum oscillations (see next section).

QUANTUM OSCILLATIONS AND FERMI SURFACE OF $ZRTE_5$

The Fermi surface (FS) of $ZrTe_5$ has been studied by several quantum oscillation studies [2–7]. However, its doping evolution has not been discussed to our knowledge. We report in Tab. II the results of previous quantum oscillations measurements (frequencies and masses) along the three crystallographic directions (a,b,c) of the orthorhombic unit cell, as well as our results on three samples from batches S_1, S_2 and S_3. As shown in Fig. 2 of the main manuscript, the angular dependence of the frequency (F) of quantum oscillations is well described by an anisotropic ellipsoid ($F = \frac{F_0}{(1+(1/A^2-1)cos^2(\theta))^{\frac{1}{2}}}$) with a Fermi momentum ratio between the long axis (b) with the a-axis equal to ≈ 12 and ≈ 8 with c-axis. The doping evolution of both anisotropies is shown in Fig. 2e) of the main manuscript and tends to increase as the Fermi energy is decreasing.

We report as well in Tab. II the carrier density deduced from quantum oscillations (n_{SdH}), the position of the last observed peak in ρ_{xx} for $\mathbf{B}//\mathbf{b}$ (B_{QL}) and the position of the transition (B_c). Measurements of the frequency of quantum oscillations along the three high axis of symmetry allow to determine $n_{SdH} = \frac{k_{fa}k_{fb}k_{fc}}{3\pi.^2}$. In the case where only the frequency along the b-axis has been measured n_{SdH} has been computed using the value of the anisotropy deduced from Fig. 2e) of the main text. We note a good agreement between n_{SdH} and n_H. An accurate measurements of n_H is challenging for our thin samples.

Ref	F_a(T)	F_b(T)	F_c(T)	$m_a(m_0)$	$m_b(m_0)$	$m_c(m_0)$	n_{SdH} (cm^{-3})	B_{QL}(T)	B_c(T)
[3]	53	4.9	27	0.020	2.7	0.077	6.5e17	–	–
[8]	–	5.2	–				5.2e17	5.2	–
[4]	46.6	4.8	29.4	0.016	1.6	0.0422	4.6e17	8	25±5
[6]	30	4	24				3.0e17	5	–
[5]	33.4	3.76	25.12	0.011	0.58	0.0617	3.2e17	3.33	–
[9]	–	0.82	–	–	–	–	4.4e16	1.0	–
[10] (S_0)	16.6	1.32	9.9	–	–	–	8.36e16	1.4	5.21
[10] (S_1)	–	1.09	–	–	–	–	6.7e16	–	6.59
[10] (S_2)	15.7	1.18	9.2	0.006	2.5	0.05	7.4e16	1.3	6.72
[10] (S_4)	–	1.29	–	–	–	–	8.6e16	–	7.25
[7]	16.7	1.1	12.3	–	–	–	8.5e16	1.2	–
[7]	15.2	1.2	13.9	0.021	6.078	0.075	9e16	1.4	8.5
S_1	5	0.33	3	0.0041	2.7	0.009	1.2e16	0.33	1.5
S_4	–	0.73	–				3.6e16	0.8	4.1
S_2	17.3	1.29	9.1	0.02	1.7	0.03	8.1e16	1.37	6.92
S_3	56.5	5.8	35.7	0.01	2	0.05	6.14e17	11.57	31±5

TABLE II: Quantum oscillations measurements in $ZrTe_5$. $F_{a,b,c}$ are the frequencies of quantum oscillations along the three crystallographic direction (a,b,c) in the orthorhombic notation. According to the Onsager relation $F_i=\frac{\hbar A_i}{2e\pi}$ where A_i is the extremal area of the Fermi surface perpendicular to the magnetic field. The value of A_i allows to determine k_a, k_b and k_c. Masses are deduced from the temperature dependence of the quantum oscillations. $n_{SdH}=\frac{k_a k_b k_b}{3\pi^2}$. B_{QL} corresponds to the position of the last quantum oscillations maximum in ρ_{xx}. B_c corresponds to the position of the metal-insulator transition.

B_{QL} IN AN ANISOTROPIC MATERIAL

In presence of a magnetic field along the z-direction, the electronic spectrum for a 3D Schr$\acute{}$odinger electrons is quantized in Landau levels with the following dispersion:

$$\epsilon(i,k_z,\pm)=(i+\frac{1}{2}\pm\frac{M}{2})\hbar\omega_c+\frac{\hbar^2}{2m_z}k_z^2 \quad (1)$$

where $\hbar\omega_c$ is the cyclotron energy, k_z and m_z are the Fermi momentum, the mass of the carrier along the z-axis, respectively, and M is the ratio of the Zeeman and cyclotron energy $M=\frac{g\mu_B B}{\hbar\omega_c}=\frac{gm_c^*}{m_0}$ with g being the g-factor, m_C^* the cyclotron energy, and μ_B the Bohr magneton. The carrier density is the sum over all the occupied states in each Landau level. For each Landau level, the number of occupied states is the product of the in-plane degeneracy (linear in field) and the 1D degeneracy along the magnetic field. n is given by: $n=\frac{1}{2(\pi l_B)^2}\sum_{i=0}^{i_{max,\pm}}[\frac{2m_z}{\hbar^2}(\epsilon_F-(i+\frac{1}{2}\pm\frac{M}{2})\hbar\omega_c)]^{\frac{1}{2}}$ where $i_{max,\pm}$ is the index of the highest occupied Landau level with a spin polarisation along the z-direction equal to $\pm\frac{1}{2}$. For $\mathbf{B}//\mathbf{b}$ M≈1 according to angular quantum oscillations [6]. When $0<M<1$, the last oscillation is observed when the (0,+) Landau level occurs: $\epsilon_F=\epsilon(i,k_z,+)$. In the case of an anisotropic ellipsoid for a magnetic field $\mathbf{B}//\mathbf{b}$, where $m_C=\sqrt{(m_a m_c)}$ and $m_z=m_b$ it occurs when B=B_{QL} with :

$$B_{QL}=\frac{\hbar}{e}(A_1^2A_2^2M)^{\frac{1}{3}}(\sqrt{2}\pi^2 n)^{\frac{2}{3}} \quad (2)$$

where $A_1=\sqrt{(\frac{m_a}{m_b})}=\frac{k_{f,a}}{k_{f,b}}$ and $A_2=\sqrt{(\frac{m_c}{m_b})}=\frac{k_{f,c}}{k_{f,b}}$. This equation applies as well to 3D Dirac materials where $M=1$ [11]. We show in Fig. 3e) of the main manuscript the result of Eq. 2, assuming $M=1$ and including the value and doping dependence of A_1 and A_2 deduced from quantum oscillations shown in Fig. 2e) of the main manuscript.

THERMAL CONDUCTIVITY OF $ZRTE_5$

We show in Fig. 1a) and b) the temperature dependence of the thermal conductivity (κ_{xx}) of S_{1b} and S_{1c}. For these low doped samples κ_{xx} peaks at around 10 K at 100 $W.K^{-1}.m^{-1}$ significantly smaller than in other semiconductors [12]. We note that the sample with the largest mobility (S_{1c}) shows the largest peak suggesting that impurity scattering affects the amplitude of the peak. The electronic contribution is estimated according to the Wiedemann–Franz law: $\kappa_{xx}^{el}=\frac{L_0}{\rho_{xx}}$=0.006$W.K^{-2}.m^{-1}$ where $L_0=2.44\text{e-}8$ $W.\Omega.K^{-2}$. This is four times smaller than the phonon contribution at the lowest temperature (T = 0.15 K). The thermal contribution is therefore purely phononic in the whole temperature

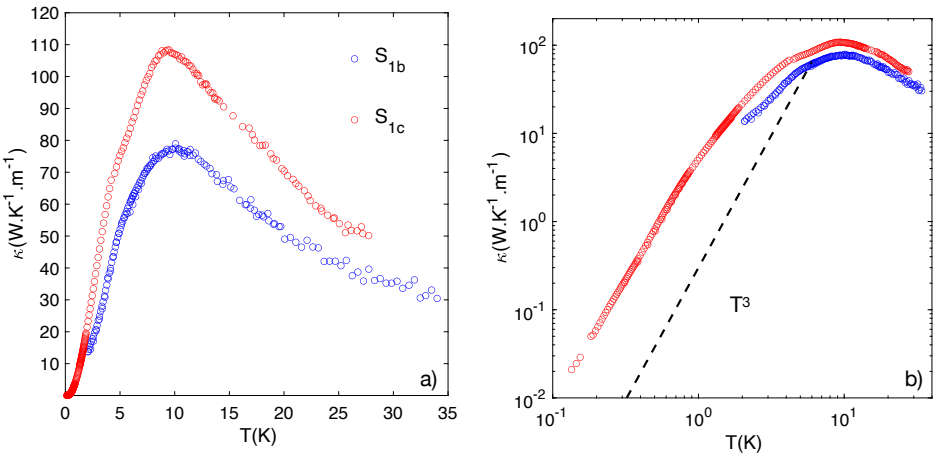

FIG. 1: **a) Temperature dependence of the thermal conductivity (κ_{xx}) for the samples S_{1b} and S_{1c}. b) Same as a) in log-log scale. The dote line is a T^3-dependence characteristic of the phonon ballistic contribution.**

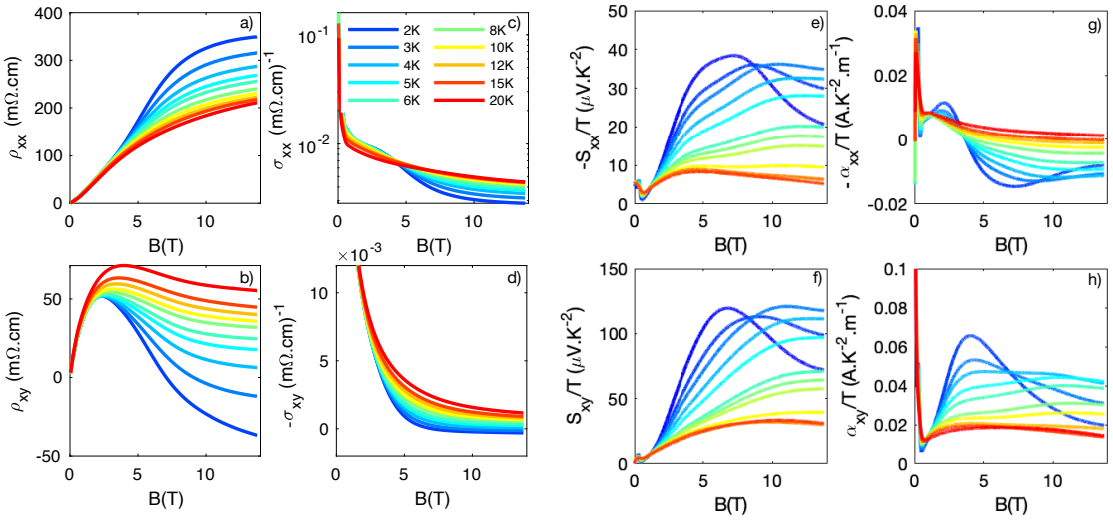

FIG. 2: **Electrical and thermoelectrical properties of samples S_{1b} from T = 2 K to 10 K : a) ρ_{xx} vs B, b) ρ_{xy} vs B, c) σ_{xx} vs B, d) σ_{xy} vs B, e) -$\frac{S_{xx}}{T}$ vs B, f) $\frac{S_{xy}}{T}$ vs B, e) -$\frac{\alpha_{xx}}{T}$ vs B, f) $\frac{\alpha_{xy}}{T}$ vs B**

range in these low doped samples. Below 0.8 K, κ_{xx} scales with T^3 as expected in the phonon ballistic regime. This is further confirmed by the estimation of the phonon mean free path ℓ_0. Extrapolating the T^3 dependence of the measured specific heat down to 6 K [13] to 0.2 K we estimate ℓ_0 to be 0.2 mm, comparable with the sample thickness.

SUPPLEMENTARY DATA ON THE ELECTRICAL AND THERMOELECTRICAL PROPERTIES OF ZRTE$_5$

We report in this section the full set of data of the electrical and thermoelectric properties of samples S_{1b} (see Fig. 2) and S_{1c} (see Fig. 3 for T = 2 K to 20 K and Fig. 4 for T = 0.15 K to 5.5 K) as well as the set of electrical transport data for S_{2c} (see Fig. 5).

In S_{1b}, S_{1c} and S_{2c} we detect a saturation of the resistivity deep inside the magnetic freeze-out regime that it is accompanied by a sign change in the Hall effect (see Fig.2b), Fig.3b), Fig.4b) and Fig.5b)). In S_{1b} and S_{1c} both S_{xx} and S_{xy} peaks close the transition (see Fig.2e-f), Fig.3e-f) and Fig.4e-f)) as recently observed across the magnetic freeze-out transition in InAs [1]. Above it S_{xx} change of sign at low temperature. The field dependence of S_{xx} is

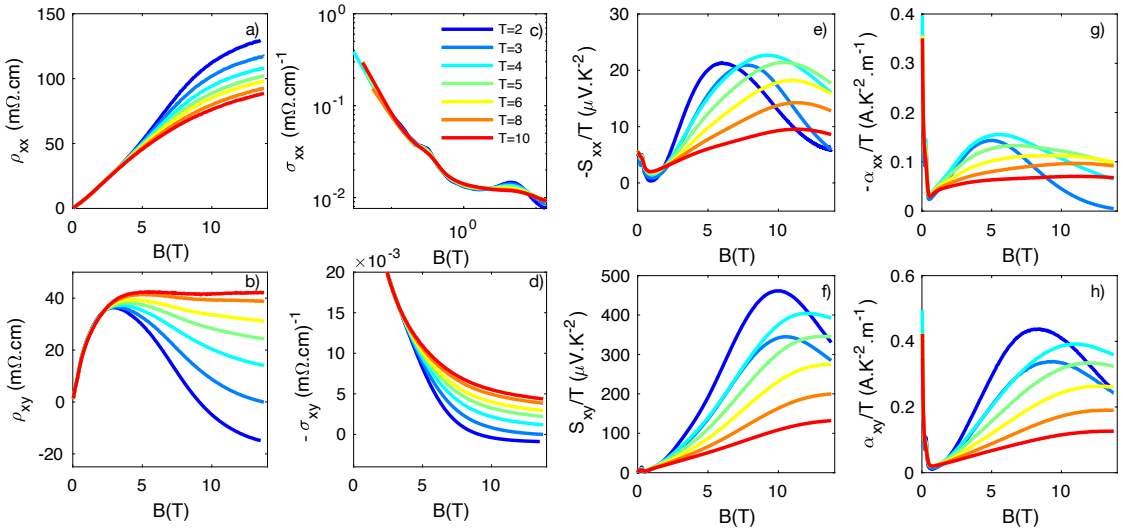

FIG. 3: **Electrical and thermoelectrical properties of samples S_{1c} from T = 2 K to 20 K : a)** ρ_{xx} **vs B, b)** ρ_{xy} **vs B, c)** σ_{xx} **vs B, d)** σ_{xy} **vs B, e)** $-\frac{S_{xx}}{T}$ **vs B, f)** $\frac{S_{xy}}{T}$ **vs B, e)** $-\frac{\alpha_{xx}}{T}$ **vs B, f)** $\frac{\alpha_{xy}}{T}$ **vs B**

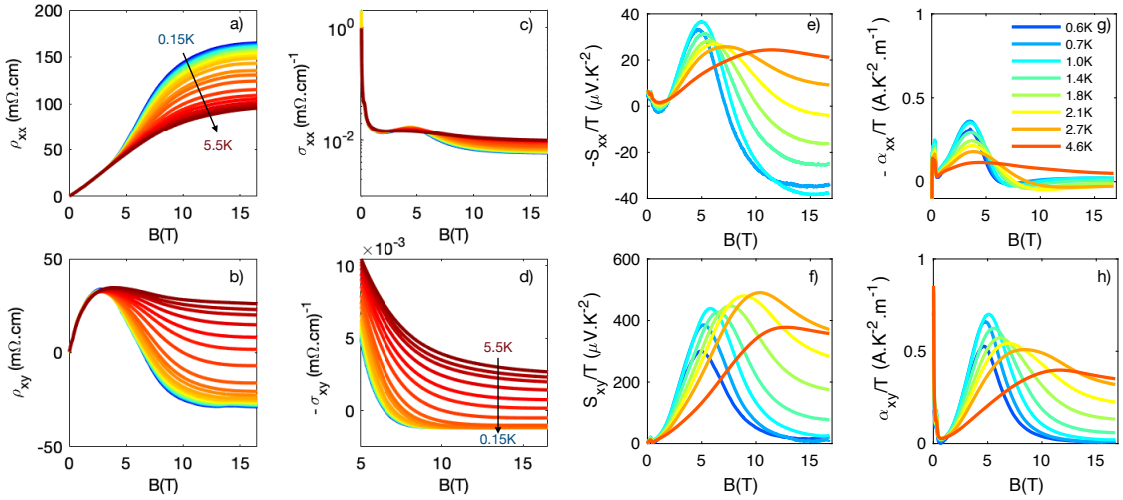

FIG. 4: **Electrical and thermoelectrical properties of samples S_{1c} from T = 0.15 K to 5.5 K : a)** ρ_{xx} **vs B, b)** ρ_{xy} **vs B, c)** σ_{xx} **vs B, d)** σ_{xy} **vs B, e)** $-\frac{S_{xx}}{T}$ **vs B, f)** $\frac{S_{xy}}{T}$ **vs B, e)** $-\frac{\alpha_{xx}}{T}$ **vs B, f)** $\frac{\alpha_{xy}}{T}$ **vs B**

qualitatively well captured by the Mott relation [14]($\frac{S_{xx}}{T} = -\frac{\pi^2}{3}\frac{k_B^2}{e}\frac{\partial \ln(\sigma(\epsilon))}{\partial \epsilon}_{\epsilon=\epsilon_F}$): this is in the region where ρ_{xx} and ρ_{xy} (and thus σ_{xx}) vary the most with both the magnetic field and temperature that S_{xx} is the largest. As a function of the magnetic field, it happens close to B_c leading to a peak in the field dependence of S_{xx} and S_{xy}. In contrast with InAs [1], where the amplitude of the peak becomes remarkably large at finite temperature ($-S_{xx}$ reaches 11 mV.K^{-1} at T = 8 K), we find here that the amplitude of the peak in S_{xx} is rather modest ($\frac{-S_{xx}}{T} \approx 20$ μV.K^{-2}) and decreases with temperature due, most likely, to the absence of phonon dragg contribution in our $ZrTe_5$ samples. The same trend is observed in the Nernst effect. We note that the amplitude of the peak in $\frac{S_{xy}}{T}$ is however significant larger than in $\frac{-S_{xx}}{T}$.

Measurements of ρ_{xx}, ρ_{xy}, S_{xx} and S_{xy} allows to compute the conductivity and thermoelectrical tensor elements σ_{xx}, σ_{xy}, α_{xx} and α_{xy} as function of the magnetic field (see on Fig.2, Fig.3, Fig.4 and and Fig.5) and as function of the temperature (see Fig.6). σ_{xx} and $-\sigma_{xy}$ both decreases by several order of magnitude. The entrance in the freeze-out regime is marked by a crossing point in σ_{xx}. Above it σ_{xx} drops and σ_{xy} changes of sign and then saturates to a non

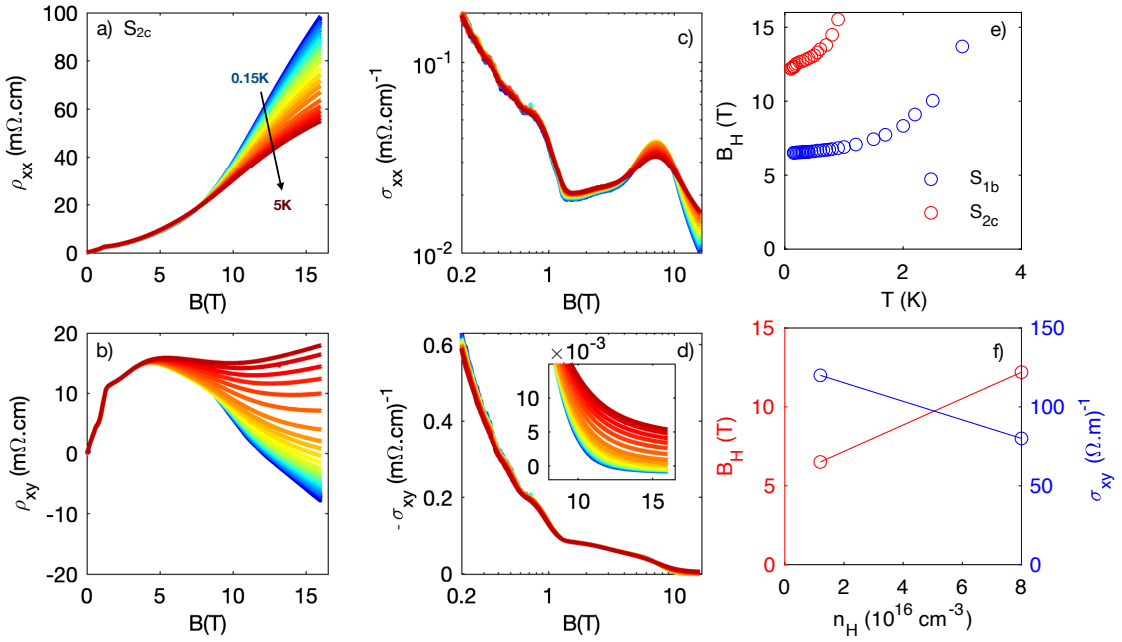

FIG. 5: **Electrical properties of samples S_{2c} from T = 0.10 K to 5.5 K : a)** ρ_{xx} **vs B, b)** ρ_{xy} **vs B, c)** σ_{xx} **vs B, d)** σ_{xy} **vs B, e) Temperature dependence of the field at which the Hall effect is equal to zero for S_{1b} and S_{2c}, f) Carrier density evolution of the low temperature value of B_H and of σ_{xy}(B=16T).**

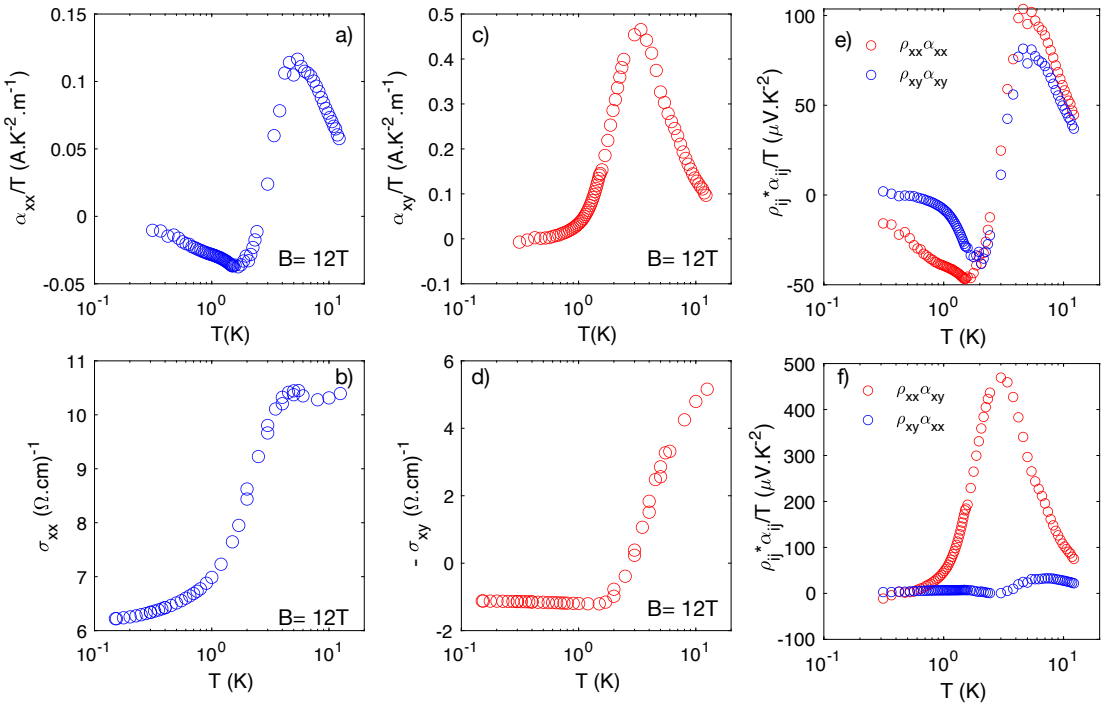

FIG. 6: **Electrical (σ_{ij}) and thermoelectrical (α_{ij}) tensor of samples S_{1c} at B = 12 T : a)** α_{xx}/T **vs T, b)** σ_{xx} **vs T, c)** α_{xx}/T **vs T, d)** σ_{xy} **vs B, e)** $\rho_{xx}\alpha_{xx}/T$ **and** $\rho_{xy}\alpha_{xy}/T$ **vs T f)** $\rho_{xx}\alpha_{xy}/T$ **and** $\rho_{xy}\alpha_{xx}/T$ **vs T.**

zero value. Above 5 K $\frac{\alpha_{xy}}{T}$ first decreases and then saturates above 1 T to value of $\approx 0.02\mu V/K^{-2}$ in good agreement with the "universal plateau" found in [8]. Below 5 K, our measurements reveals however a profound change. Both $\frac{\alpha_{xx}}{T}$ and $\frac{\alpha_{xy}}{T}$ peak to a value much larger than the plateau value. As discussed in the previous paragraph we attribute it to the magnetic freeze-out effect.

The saturating Hall conductivity point to an AHE contribution that can have an intrinsic or extrinsic origin. In the case of a skew scattering (extrinsic origin) σ_{xy}^{A}=N$_S$e$\frac{g^*\mu_B}{E_1}$ where E_1= is the band gap, N$_S$ is the density of scattering centers. In this framework a sign change of the Hall effect is expected when B=B$_H$=$\frac{n}{N_S}\frac{E_g}{g^*\mu_B}$. As the temperature is lower n is decreasing in the magnetic freeze-out regime and B$_H$ does so (see Fig. 5e)). We show on Fig. 5 the low temperature values of B$_H$ and σ_{xy} for S$_{1b}$ and S$_{2c}$. Assuming that N$_S \approx n$ we found that $\sigma_{xy} \approx 1$ $(\Omega.cm)^{-1}$ in good agreement with the amplitude of the measured σ_{xy}. In the zero temperature limit we find in S$_{1b}$ that B$_H$=6 T which would imply that $\frac{n}{N_S}$=0.3 comparable with the drop of charge carrier estimated from the thermopower (of about 0.125) across the freeze-out.

According to these two estimations the freezing of the charge carrier is therefore not total which is further support by the saturating behavior of ρ_{xx}. Similar effects have been observed in the freeze-out regime of InAs [1] and have been attributed to potential fluctuations. In presence of large-scale potential fluctuations the tail of the (0,-) Landau level has width, Γ, given by : $\Gamma = 2\sqrt(\pi)\frac{e^2}{\epsilon r_s}(N_S r_s^3)^{\frac{1}{2}}$ where $r_s \propto \sqrt(\frac{a_B}{n^{\frac{1}{3}}})$ is the screening radius and N$_S$ an estimate of the impurity concentration. Assuming that $n \approx N_S$ we found $\Gamma \approx 6$ meV. In contrast with other narrow gap semi-conductors where $\Gamma << E_F << \Delta$, in ZrTe$_5$ the magnetic freeze-out occurs in the case where $\Gamma \approx E_F \approx \Delta$. Across the transition electrons shift to the conduction band to a shallow band of width Γ comparable with the band gap. The subsequent overlap bands implies that the carrier density is not vanishing, even at the lowest temperature, inducing a saturation of n_H and ρ_{xx} even deep in the freeze-out regime. As the doping increasing, Γ is increasing and the transition becomes less and less defined.

DETERMINATION OF THE DIELECTRIC CONSTANT

As ZrTe$_5$ is a conductor, its dielectric constant is strongly perturbed by the free carriers conductivity and it cannot be directly measured with transport techniques. However, it can be determined from the optical response of the material, once the free charge carrier contribution is isolated.

In the harmonic approximation, the frequency-dependent dielectric function $\varepsilon(\omega)$ of a material is described by the Drude-Lorentz equation:

$$\varepsilon(\omega) = \varepsilon_\infty - \frac{\Omega_p^2}{\omega^2 + i\omega/\tau} + \sum_j^{(ph)} \frac{\Delta\varepsilon_j\,\Omega_j^2}{\Omega_j^2 - \omega^2 - i\gamma_j\omega} \quad , \tag{3}$$

where ε_∞ is the contribution from electronic transitions; the second term is the Drude contribution characterized by a plasma frequency (Ω_p) and scattering rate (τ^{-1}); and the last term is the summation over the dielectric susceptibility of each phonon (j) having a resonance frequency Ω_j, a linewidth γ_j and a dielectric strenght $\Delta\varepsilon_j$. Subtracting the Drude contribution out of Eq. 3, we get the dielectric constant simply by setting $\omega = 0$:

$$\varepsilon_{dc} = \varepsilon(0) = \varepsilon_\infty + \sum_j \Delta\varepsilon_j \quad . \tag{4}$$

Therefore, to obtain the dielectric constant of a material we simply have to obtain the values for ε_∞ and each $\Delta\varepsilon_j$, not forgetting to isolate and eliminate the free carriers contribution in our way.

We calculated ε_{dc} using two different procedures. Our first method consists in fitting the reflectivity of the material with the dielectric function of Eq. 3 and Snell-Descartes formula:

$$R = \left|\frac{n-1}{n+1}\right|^2 = \left|\frac{\sqrt{\varepsilon}-1}{\sqrt{\varepsilon}+1}\right|^2 \quad . \tag{5}$$

This method yield direct values for the quantities we are looking for but has the drawback of assuming that phonons are harmonic and mobile carriers are described by the Drude formula. An example for the fitting of the reflectivity is shown in the inset of the left panel in Fig. 7. The thin blue line in the main panel shows the dielectric function extracted from this method. The Drude contribution is the thick cyan line, which when subtracted from the full dielectric function produces the thin red line. The zero frequency extrapolation of this line is the dielectric function

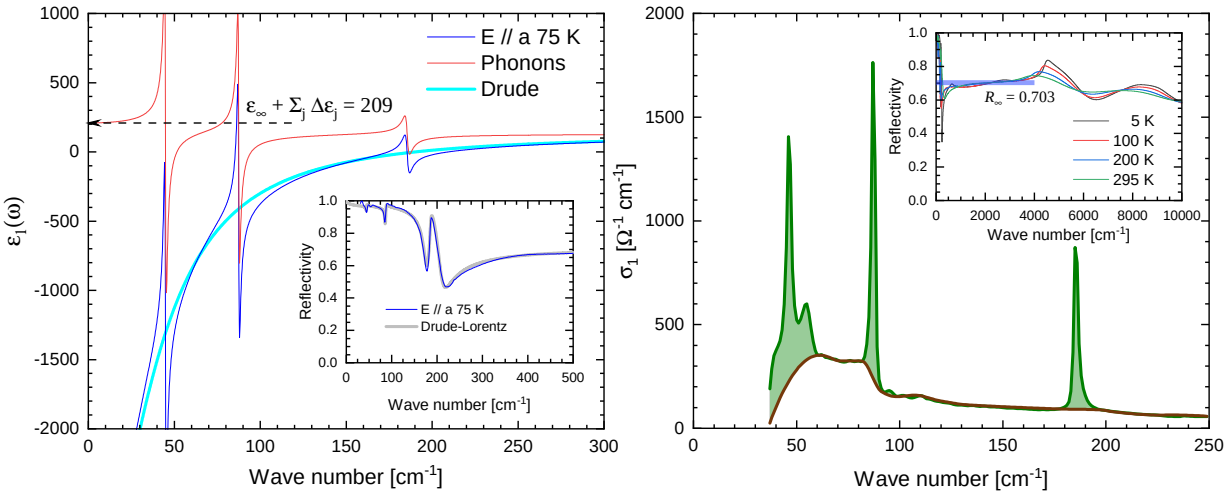

FIG. 7: Left-hand side: The inset shows the $E \parallel a$ reflectivity for $ZrTe_5$ at 75 K. The thin blue line is the data and the thick gray line is a fit with the Drude-Lorentz dielectrict function. The thin blue line in the main panel is the thus obtained real part of the dielectric function. The thick cyan line is the Drude contribution to ε. Once it is subtracted from the full response, we obtain the red line composed of high frequency electronic transitions and phonons. The zero-frequency extrapolation of this line gives the dielectric constant. Right-hand side: The inset shows the $ZrTe_5$ reflectivity for a few temperatures. The thick blue line represents a region where R is flat and from which we can safely extract a value for $\varepsilon_\infty \approx 130$. The main panel shows the Kramers-Kronig obtained real part of the optical conductivity. The thick brown line is taken as an electronic background. The shaded areas and the peak positions allows us to calculate each phonon contribution to the dielectric constant.

we are looking for. Of course, this whole graphic process is only illustrative. To obtain the dielectric function it suffices to sum up the fit-determined values for the dielectric strengths of each phonon and ε_∞.

Our second method is still based on Eq. 4 but does not assume that the phonon lineshapes are harmonic nor that electrons follow the Drude response. It is based on the oscillator strength for a phonon, calculated from the real part of the optical conductivity (σ_1):

$$\int_{ph} \sigma_1(\omega) d\omega = \frac{\pi}{2} \varepsilon_0 \Delta\varepsilon\, \Omega^2 \quad , \tag{6}$$

where the integration limits correspond to each phonon frequency range. In this method, we first extract ε_∞ from the reflectivity data, as shown in the inset of the right-hand side panel in Fig. 7. Note that around 2000 cm^{-1} the reflectivity is fairly flat ($R_\infty \approx 0.7$) as shown by the thick blue line. We are using R_∞ to indicate that it is related to ε_∞. A flat reflectivity implies that the dielectric function is real and so is the refraction index. It then becomes trivial to invert Eq. 5 to obtain ε_∞.

In a second step, we calculate the optical conductivity from Kramers-Kronig relations, obtaining the data shown in the main panel at the right-hand side of Fig. 7. We then subtract an arbitrary electronic background indicated by the thick brown line and calculate the area for each phonon, shown by the shaded green areas. From this areas, we extract each phonon dielectric strength using Eq. 6 and we have our dielectric constant.

For the example given in Fig. 7, we obtain $\varepsilon_{dc} = 209$ for the dielectric function method and $\varepsilon_{dc} = 290$ for the spectral weight method. In addition to this difference, we also took into account fitting errors and different electronic baselines in order to calculate our confidence range.

[1] A. Jaoui, G. Seyfarth, C. W. Rischau, S. Wiedmann, S. Benhabib, C. Proust, K. Behnia, and B. Fauqué, npj Quantum Materials **5**, 94 (2020), ISSN 2397-4648, URL `https://doi.org/10.1038/s41535-020-00296-0`.

[2] G. N. Kamm, D. J. Gillespie, A. C. Ehrlich, T. J. Wieting, and F. Levy, Phys. Rev. B **31**, 7617 (1985), URL `https://link.aps.org/doi/10.1103/PhysRevB.31.7617`.

[3] M. Izumi, T. Nakayama, K. Uchinokura, S. Harada, R. Yoshizaki, and E. Matsuura, Journal of Physics C: Solid State Physics **20**, 3691 (1987), URL https://doi.org/10.1088/0022-3719/20/24/011.
[4] Y. Liu, X. Yuan, C. Zhang, Z. Jin, A. Narayan, C. Luo, Z. Chen, L. Yang, J. Zou, X. Wu, et al., Nature Communications **7**, 12516 (2016).
[5] G. Zheng, J. Lu, X. Zhu, W. Ning, Y. Han, H. Zhang, J. Zhang, C. Xi, J. Yang, H. Du, et al., Phys. Rev. B **93**, 115414 (2016), URL https://link.aps.org/doi/10.1103/PhysRevB.93.115414.
[6] J. Wang, J. Niu, B. Yan, X. Li, R. Bi, Y. Yao, D. Yu, and X. Wu, Proceedings of the National Academy of Sciences **115**, 9145 (2018), ISSN 0027-8424, https://www.pnas.org/content/115/37/9145.full.pdf.
[7] S. Galeski, T. Ehmcke, R. Wawrzyńczak, P. M. Lozano, K. Cho, A. Sharma, S. Das, F. Küster, P. Sessi, M. Brando, et al., Nature Communications **12**, 3197 (2021), ISSN 2041-1723, URL https://doi.org/10.1038/s41467-021-23435-y.
[8] J. L. Zhang, C. M. Wang, C. Y. Guo, X. D. Zhu, Y. Zhang, J. Y. Yang, Y. Q. Wang, Z. Qu, L. Pi, H.-Z. Lu, et al., Phys. Rev. Lett. **123**, 196602 (2019), URL https://link.aps.org/doi/10.1103/PhysRevLett.123.196602.
[9] W. Zhang, P. Wang, B. Skinner, R. Bi, V. Kozii, C.-W. Cho, R. Zhong, J. Schneeloch, D. Yu, G. Gu, et al., Nature Communications **11**, 1046 (2020).
[10] F. Tang, Y. Ren, P. Wang, R. Zhong, J. Schneeloch, S. A. Yang, K. Yang, P. A. Lee, G. Gu, Z. Qiao, et al., Nature **569**, 537 (2019).
[11] T. Liang, Q. Gibson, J. Xiong, M. Hirschberger, S. P. Koduvayur, R. J. Cava, and N. P. Ong, Nature communications **4**, 2696 (2013).
[12] J. W. Vandersande and C. Wood, Contemporary Physics **27**, 117 (1986), https://doi.org/10.1080/00107518608211003, URL https://doi.org/10.1080/00107518608211003.
[13] R. Shaviv, E. F. Westrum, H. Fjellvag, and A. Kjekshus, Journal of Solid State Chemistry **81**, 103 (1989), ISSN 0022-4596.
[14] J. M. Ziman, *Principle of the theory of solids* (Cambridge University Press, 1972).